Egypt. J. Chem. **Vol. 65,** No. SI:13B pp. 981 -993 (2022)

Egyptian Journal of Chemistry

http://ejchem.journals.ekb.eg/

Utilizing Laser Spectroscopic Investigations to Determine the Current Conditions of Hetep Heres' Pyramid in Giza, Egypt.

Omar Mohammed Abd El Hameed [1], Aalaa Gamal Ali[1], Diaa Atta[2, 3]

[1] *Conservation Department, Faculty of Archaeology, Cairo University, 12613 Giza, Egypt.*

[2] *Spectroscopy department, Physics Research institute, National Research Centre, 33 El Behooth St., Dokki, Giza, Egypt, Affiliation ID: 60014618.*

[3] *Nonlinear optics and fluorescence Unit-National Research Centre-Dokki, Cairo 12622, Egypt, Affiliation ID: 60014618.*

Abstract

Giza plateau in Egypt is famous for its pyramids and tombs which were built and carved into the rock. The pyramid of Queen Hetep Heres, the mother of King Khufu, encountered several erosion factors. From a simple visual examination, it is noted that Hetep Heres' pyramid has many problems that affect its sustainability. Different samples have been taken from the eroded areas. The external state that was investigated by a stereo microscope shows erosion and damage. The internal and structural states were investigated by scanning electron microscope, X-ray diffraction, EDAX, and laser-based Raman microscope. This study confirms the need to interfere with the surrounding urban area to decrease the frictions and the strong need to continue developing the Giza Plateau to decrease the environmental effects on the whole archeological buildings found in one of the most important plateaus in the world.

Keywords: Raman micro-spectroscopy; Hetep Heres' Pyramid; Building materials; Deterioration factors; Laser spectroscopy.

1. Introduction

Giza plateau is crowded with pyramids and tombs which were established for thousands of years on its rocks.

King Khufu has one of the world's wonders established and carved through the Giza Plateau. King Khufu established a side pyramid for his mother queen Hetep Heres (I). The pyramids are considered one of the most important buildings in the world due to their historical depth and unique architecture.

The glorious Egyptian pyramids are part of the considerable buildings situated on the plateau of a limestone ridge overlooking the productive landscapes of the Nile valley. By the middle of the twenty-sixth century BC, the fourth-dynasty pharaoh Khufu, has been select the plateau as the location of his wonder [1].

The first time that one of the ancient Egyptian kings decided to establish his unique project over the human ages on the Giza plateau was Khufu. The son of Sneferu and the first Hetep Heres chose this place because its suitable bedrock formed of hard limestone [2].

As illustrated in Figure 1 the Pyramid of Hetep Heres is one of the three queens' pyramids located easterly from the Great Pyramid, in the Giza necropolis.

As illustrated in Figure 1 the Pyramid of Hetep Heres is one of the three queens' pyramids located easterly from the Great Pyramid, in the Giza necropolis.

Hetep-Heres I is the daughter of Huni and the wife of the first king of Dynasty IV, Sneferu the mother of Khufu [3]. The Pyramid of Hetep Heres was built during the Fourth dynasty of Egypt. It has a base of 49.5 m wide and originally a height of 30.25 meters; the pyramid has lost two-thirds of its original height [4]. The entrance of the pyramid is located in the north wall, followed by a descending corridor that turns to the right and ends with a small burial chamber that was cut into the rock.

1.1. Local characteristics:

The Pyramid of Hetep Heres is settled in the north-west section Giza plateau. The site of the Giza plateau was selected carefully according to certain criteria: low tectonic and low seismicity [5], high altitude to withstand the effect of Nile overflooding, good building rocks for long lasting and remaining over ages, steady form, and steady constructive layout [5].

*Corresponding author e-mail: DE.Kamal@nrc.sci.eg.

Receive Date: 11 August 2022, Revise Date: 19 August 2022, Accept Date: 31 August 2022

DOI: 10.21608/EJCHEM.2022.155708.6727

Fig. 1. (a) Giza plateau with the three main pyramids (Khufu, Khafra, and Menkaura), (b) Details of the pyramid of Queen Hetep Heres to the east of Khufu's pyramid, (c) The pyramid of queen Hetep Heres.

As it is clear in Figure 2 In the early ages, the Giza plateau was connected to the Moqattam mountain. The two sites have the same geological structure as they were composed of central cretaceous depositions surrounded by Eocene depositions “pivot directed from the east-northern to the west-southern”. This pivot is unified with the gravitational centers of the three pyramids' [6,7]. Middle Eocene Moqattam formation is composed mainly of white fossiliferous limestones with some marly limestone beds [7].

The three main components of the Giza plateau can be distinguished as follows: First, Nummulite depositions, which form a large part of the bases of the Khufu and Khafra pyramids. Second, Shoal and shoal reef depositions at the bottom part of the Sphinx ditch and along the road from the Sphinx temple up to the pyramids. Third, back bank depositions that form the body of the Sphinx statue and the southern part of the pyramids plateau [8,9]. Table 1 show the stratigraphic column for the two main formations (upper and middle Eocene) of the pyramid plateau.

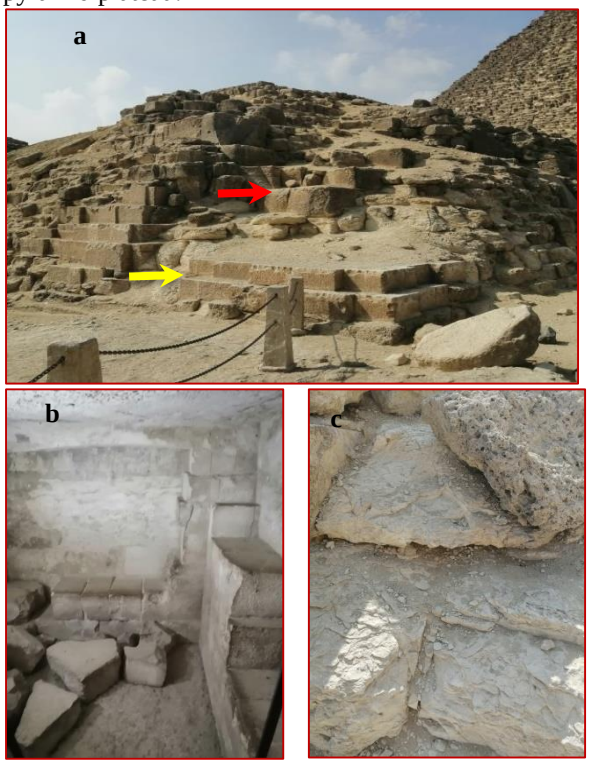

Fig. 2. (a) General view of Hetep Heres pyramid showing the main construction blocks "red arrow" and casing stones "yellow arrow", (b) the bed rock of the plateau, (c) detail of the rock-cut burial chamber.

1.2. Climatic characteristics:

To form a clear image of the state of the archaeological building materials in the pyramid of Hetep Heres, It's necessary to clarify the effect of climatic factors represented in the rate of rainfall, temperatures, the effect of wind, and humidity.

The Egyptian weather is like a desert, its summer is depicted as hot-dry while its winter is moderate with little rainfall. From the rainfall data, Egypt is divided into three regions, among them Giza is located in is the second region, which is a region with little rainfall with an average between 25 and 100 millimeters.

The temperature in Cairo for example, is alternating from approximately 18 ºC on the coldest day in January to the hottest day with approximately 36 ºC in July. The daily and seasonal temperature range increases sharply in the deserts of Egypt as in the Giza plateau, with the average temperature reaching 40 °C during day hours, while it drops to about 7 °C after sunset. The fluctuation in temperature increases the activity of the thermal weathering processes that lead to the granular disintegration inside the stones. It also contributes to the activity of the salt weathering processes,

especially the growth of salt crystals and thermal expansion [10].

Some Egyptian districts suffer strong wind, especially those districts parallel to the Red Sea (annual average of 8.0-10.0 m/sec) and Mediterranean coasts (annual average of 6.0-6.5 m/sec) [11]. The most important local winds that the Egyptian lands are exposed to winds are known as the Khamaseen winds, and the month most exposed to the Khamaseen winds is the month of April. The Khamaseen is characterized by hot winds and carries large quantities of sand and dust that negatively affect the archaeological buildings [12]. Regarding relative humidity, it rises clearly along the Mediterranean coasts throughout the year and the Red Sea coasts, especially in the summer. While the humidity in the air decreases sharply when the country is exposed to the blowing of the Khamaseen winds during the period between March and June.

The negative effect on the archaeological buildings is in the event of fluctuations between temperature and humidity, as high temperatures and low humidity lead to an increase in the activity of saline weathering processes, where the wet processes occur in the early morning and then followed by rapid evaporation when the temperature rises during the day [13]. While the increase in temperature and increase in humidity values at the end of spring and early autumn also results in the activity of dissolving and carbonization processes and hydration of salts in areas where limestone and sand are present and resulting in dissolution pits and honeycombs phenomena [12].

Besides the effect of relative humidity, the site of the great Sphinx (southwest of Hetep Heres pyramid) has been negatively affected by increasing the west water that leaking from the surrounding inhabiting assemblies and irrigation canals near the Giza plateau [7].

1.3. Spectroscopic analysis techniques:

Molecular spectroscopy like FTIR and Raman is a powerful characterization tool, especially if the issue is the recognition of the chemical structure and the nascent changes during the reactions for vast spectra of scientific investigations from bio materials to organic and inorganic compounds passing with polymers and nano structures [14-19].

Table 1.

Show the stratigraphic column for the two main formations (upper and middle Eocene) of the pyramid plateau [9]

Stratigraphy	Formation		Components
Upper Eocene	Maadi Group	• Ain Musa Mb. • Carolia Bed • Wadi Garawi Fr. • El-Qura Fr.	• Sandy limestone • Carolia Placunoides biohorizon • Shally marl layers and thin-bedded marly limestone • Agillaceous limestone and gypseous marl
Middle Eocene	Mokattam	• Observatory Formation • Upper • Middle • Lower	• White gray marly limestone • Limestone marl complex sequence-Nummulite Bank • dark gray dolomitic limestone • Nummulite white limestone

Other spectroscopic tools like fluorescence are regarded as another important pillar in its both branches steady-state and time decay [18-20]. A perfect and green spectroscopic tool is the molecular dynamics which serves in identifying the inter-molecular spacing, electrostatic potential mapping, HOMO-LUMO values and more [21-24].

Over around 3 decades Raman spectroscopy turned into one of the most important analysis tool in cultural heritage and artists materials as one from the none destructive or inoffensive characterization techniques. In comparison with the different molecular spectroscopic techniques, the laser-based Raman spectroscopy affords forthright recognition of the chemical structure with a better and direct appearance for the inorganic and organic molecules [25]. So, laser-based Raman spectroscopy turns into one of the characterization pillars of heritage research besides FTIR [26-29].

Despite the advances and the added value to the Raman spectroscopy laser usage as a source instead of the conventional lamp but the concentrated power of the laser spot could damage the sample or degrade the area of measurements which also could lead to misleading data. Hence adjusting and optimizing the laser power and focal volume is a crucial point in Raman analysis.

The most selected lasers in ancient samples are the blue, green, and red lasers, while the infra-red lasers could be harmful because of their thermal effect so one should be very careful during Raman measurements using this laser line. Another point is the sample color as Raman spectroscopy is based on excitation beam scattering, so the absorption of the exciting beam should be very limited or zero. In this regime it is highly recommended to not use a laser with a wavelength close to one of the used colors in the paints that as high excitation beam absorbed in the sample as less scattering of the incident laser beam which leads to very weak Raman bands.

Also as more absorbing the laser more localized heating of the exposed area, this leads to sample damage and changing in the chemical structure.

With the advances and fast development of nano technology in the lasers and CCD detectors through the last decade Raman spectroscopy developed to Raman micro-spectroscopy transferring the Raman to the new era of Raman mapping, which serves as a heaven tool for the culture heritage [29,30].

Recently the dependence on molecular modeling in assigning the molecular spectroscopy spectra became the trend [22,31]. The issue of matrix effect and the band shift according to the presence of such functional group or element could be easily assigned with the molecular modeling if the correct method and basis set were selected. The same if the change in the surrounding molecules as the usage of different salvations could be easily studied using Molecular modeling [21,24]. Moreover much other valuable information could be extracted like the electrostatic potential surrounding the studied molecule [24]

2. Materials and Methods:

2.1. Sampling:

This investigation was performed by taking three small samples as presented in Figure 3, from the spontaneously dilapidated and partially separated parts due to different weathering factors of the main building material from the Hetep Heres pyramid.

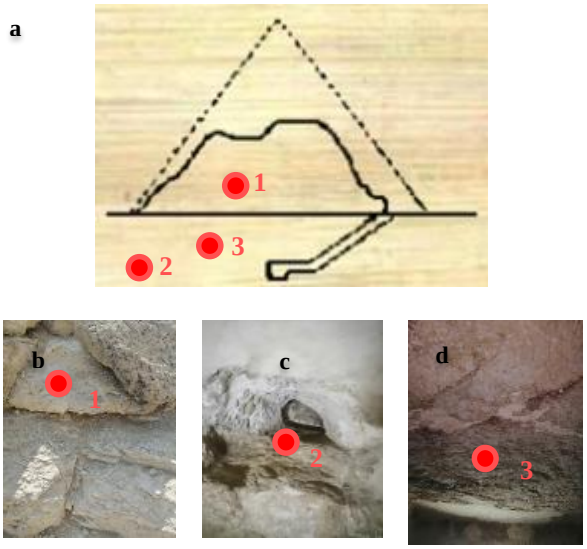

Fig. 3. Shows (a) the places of taken samples from the pyramid of Hetep Heres, (b) sample No. 1 from outside constructed part of the pyramid, (c) sample No. 2 from inside the burial chamber (the mother rock of the area), and (c) Sample No. 3 from the corridor leading to the burial chamber.

2.2. Analytical Methodology:

The importance of examinations and analysis is due to form a complete image of the components and preservation state of the studied samples.

2.2.1 Stereo microscope:

The examination was carried out by a Leica MZ6 provided with a camera (Leica MC 120 HD), with magnification ranges from 8 to 25x.

2.2.2 Imaging and analysis using Raman:

Laser-based Raman confocal microscope from Witec-Ulm Germany model Alpha300 RA/S, was utilized to record the Raman shift spectra and imaging. The Alpha 300 RA/S is coupled with bright field microscope for recording and monitoring the surfaces optically. For bright field imaging an EC Epiplan-Neofluar HD 50X objective from Zeiss was utilized with white LED illumination.

Raman spectra were smoothed and de-convoluted using self-written routines. A 100x Ziss objective has been utilized in the scattered laser collection. For laser power optimization the edge of the sample was exposed to different laser powers with an exposure time of 60 s, then the exposed point was examined optically by the confocal microscope illuminated with white LED. The optimum laser power is the highest power which did not cause any blackness to the sample. For samples S1, and S3 the laser power was optimized to 4 mW during single point measurements with 150s accumulation time. By bright field microscope, a flat area were selected for Raman imaging, this laser power caused blackness on the surface of sample S2 so the optimized power for this sample is only 1.2 mW. All areas were divided into 150 by 150 points, with pinning time 1s per point. The resolving part in the spectrograph was 600g/mm grating with BLZ= 500 nm, the laser power increased to 50 mW. The introduced maps represent the distribution of such peak after averaging the peak intensities at the center with band width 5 cm^{-1} then the intensity values for each get color-coded. The counts lower than 5 counts were coded with black color as the background, while the maximum counts coded with yellow. The color coding has been done using project 5 software from Witec- Ulm- Germany

The optical images have been recorded with a bright field optical microscope using collimated white light as a laser-like source.

2.2.3 Scanning electron microscope with EDX:

The FEG Quanta 250 is equipped with an energy dispersive spectrometer for elemental analysis on a microscopic scale.

2.2.4 X-ray diffraction:

XRD is always useful in characterizing the mineralogical structure of investigated samples by using X-Ray diffraction equipped with monochromator, and Cu-radiator at 45 K.V., 35 M.A. with scanning speed 0.03 °/sec.

3. Results and Discussion

3.1. Stereo microscope:

Figure 4 presents the stereo microscope images that clarify the weak internal composition of S1 and S2, due to the presence of voids, organic substances, fossil remains, and salt crystallization, especially in S2 which was taken from the burial chamber.

3.2. Imaging and analysis using Raman:

3.2.1. Bright field imaging:

Bright filed imaging could give an overview of the surface and its diversity.

Despite the nature of the sample and the irregularity of its surfaces, the bright field microscope snapshot 320 µm × 320 µm of the sample surface as it is presented in Figure 5. The images show a difference in color and homogeneity of the three samples which assure either the different origins of the rocks or the effect of environment on the rocks, also inhomogeneity in the samples were noticed. Hence such molecular or chemical mapping will give some information about those differences

3.2.2. Raman examination:

Raman imaging shows: First, the difference in the general color of each sample. The colors range from the light color of S1 (external sample), the mixed colors between light and dark in S3 (corridor's sample) and finally, the dark color in S2 (burial chamber's sample).

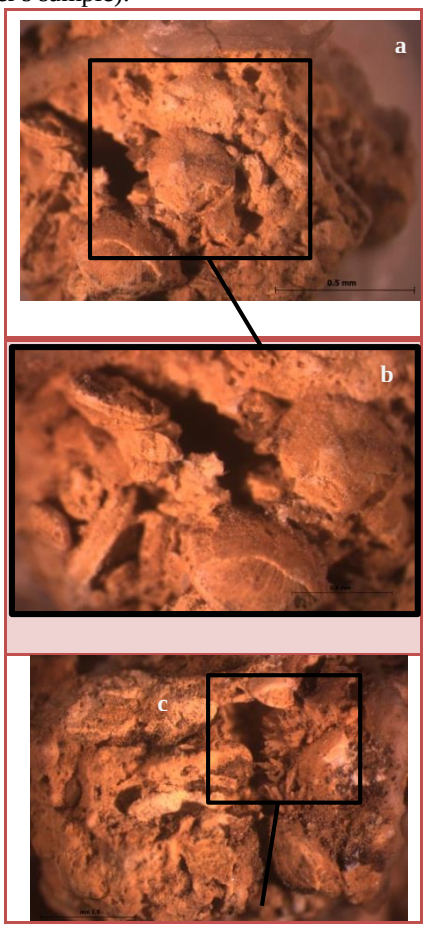

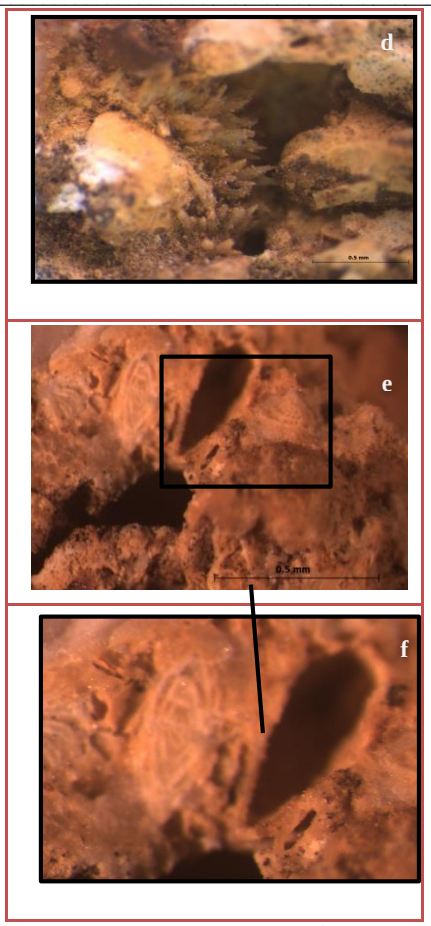

Fig. 4. Stereo microscopic micrographs of samples (a) S1, (b) enlargement of detailed area from S1 showing fossils and salt crystallization, (c) S2, (d) enlargement of detailed area from S2 showing fossils and salt, (e) another area of S2, and (f) enlargement of detailed area from S2 showing Bioclast < 2mm

Second, the proportion and diffusion in the presence of both calcite (light color) and the clay minerals (dark color), indicate that S3 has the largest number of various minerals that are explained by chemical transformations of some unstable minerals into others and these minerals not presented in S2, this indicates the difference of the source of each sample.

Optical images in Figure 5, present that the samples are different in color and color distribution; this means that the chemical structure of these samples are different, laser-based Raman micro-spectroscopy has been utilized in this regime. it is noticed a combined band in the region from 200 cm^{-1} to 320 cm^{-1} this de-convolution clarify 3 bands in the first region and 4 bands in the second region.

Through the Raman spectra of sample S1, it has been noticed, that the calcite band at 1085 cm^{-1}, kaolinite at 200 cm^{-1}, and the de-convoluted band at 269 cm^{-1}. Also, calcite have been detected through the Raman de-convoluted band at 278 cm^{-1}, also the bands at 713 cm^{-1}, and the de-convoluted bands at 247 and 1308 cm^{-1} could be attributed to dolomite. Lead compounds at 62 and 141 cm^{-1} for Pb_3O_4, at 72

and 92 cm^{-1} for PbO, and at 110 cm^{-1} for $2PbCO_3$•Pb $(OH)_2$, also carbon black detected at the de-convoluted bands 1333 and 1361 cm^{-1}, both lead compounds and carbon could be from the environmental pollution.

Figure 6(a) presents Raman spectra of sample S1, while Figure 6(b) clarifies that some bands appeared in S2 like S1, the bands at 1085, 247, 65, 77, 94, 110, 1333, and 1361 cm^{-1} which are attributed to Calcite, Hematite, Pb3O4, PbO, 2PbCO3• Pb (OH)2, PbO and Graphite. Additional bands clear in the spectra of S2, extra bands for hematite at 221, 286, 660, and 819 cm^{-1} also extra band for carbon at 1341 cm^{-1}. The Raman spectrum of this sample is not limited to the mentioned bands but another band at 282 cm^{-1} could be attributed to Calcium carbonate. Other bands at 382 and 551, also group of bands at 1066, 1099 and 1200 cm^{-1} which were attributed to silicon hydroxide, silicon oxide and silicon dioxide respectively.

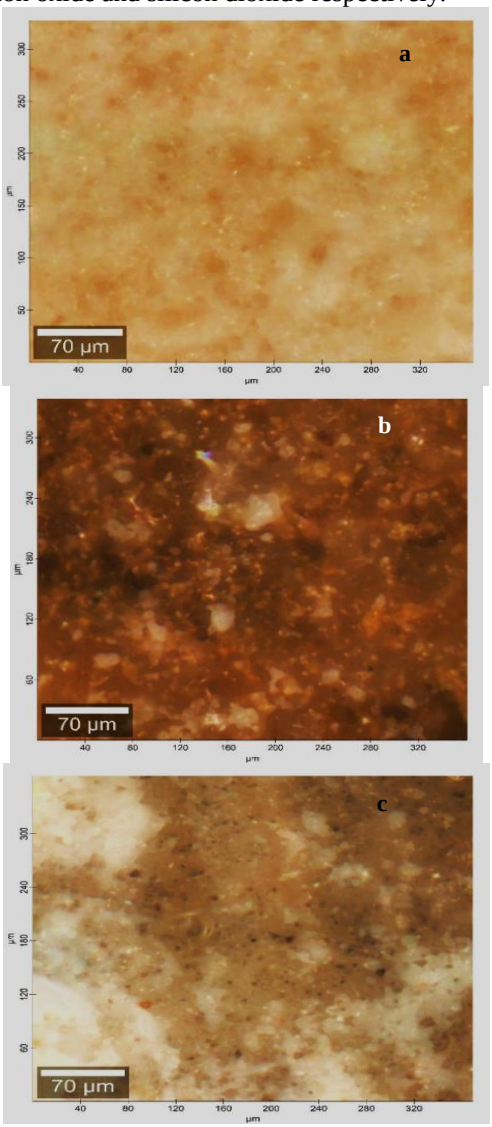

Fig. 5. Bright field image of (a) S1, (b) S2, (c) S3 with 50X objective EC Epiplan-Neofluar HD from Zeiss.

Other minerals appeared in this sample like kaolinite at Raman shifts 400, 473, and 750 cm^{-1}. Also, bands at 135 and 605 cm^{-1} could be attributed to Anhydrite. Two groups of Raman shifts detected at 174, 304, 729, and 1141 cm^{-1} together with 330, 505, 645, 763, and 1113 cm^{-1} could be attributed to the presence of Dolomite and Albite respectively. Raman shifts to 230, 675, 746, 700, 1029, and 1067 cm^{-1} could be attributed to the presence of Actinolite. Other minerals detected in this mineral rich sample, that at 557 and 1161 cm^{-1} which could be regarded to refer to Aluminum silicate, and that at 440, 835, 849, and 1042 cm^{-1} which could be ascribed to the presence of lead sulfide.

The presented Raman spectra in Figure 6(c) shows that, sample S3 is not reach like S2 but we could find a common bands with S1 and S2 like that bands at 1086 cm^{-1} (1cm^{-1} from 1085cm^{-1}), 278, 713, 1306 cm-1 (only 2cm^{-1} 1308 cm^{-1}), 62, 1329 cm^{-1} (4 cm^{-1} from 1333cm^{-1}), and 1342 cm^{-1} (shifted from 1341 and 1333 cm^{-1}). A complete assignment has presented in table 2.

3.2.3. Raman Mapping:

The recorded Raman spectra at an arbitrary point show the compositions of the tested samples, but what about the distribution of those constituents over the surface of the samples?

To answer this question Raman mapping has been done and some Raman maps of some selected Raman bands will be presented in this section.

Figures 7, 8, and 9 shows the Raman mapping of samples S1, S2, and S3, the intensities of the scattered laser from sample S2 are lower than that in S1 and S3, this could be attributed to the used laser power with the tested samples as described before in the experimental section.

Figure 7 presents the confocal Raman mapping of the sample S1 the images from (a) to (g) represents the distribution of the Raman bands over the tested area. Figure 7(a) presents the distribution of the Calcite mineral with count rate from 5 counts up to 270 counts the dominating colors over the map is cyan and green which represents counts around 100 and 135 counts. In some regions blue and color representing around 180 counts. This means continues and homogeneous distribution of the Calcite over the sample S1.

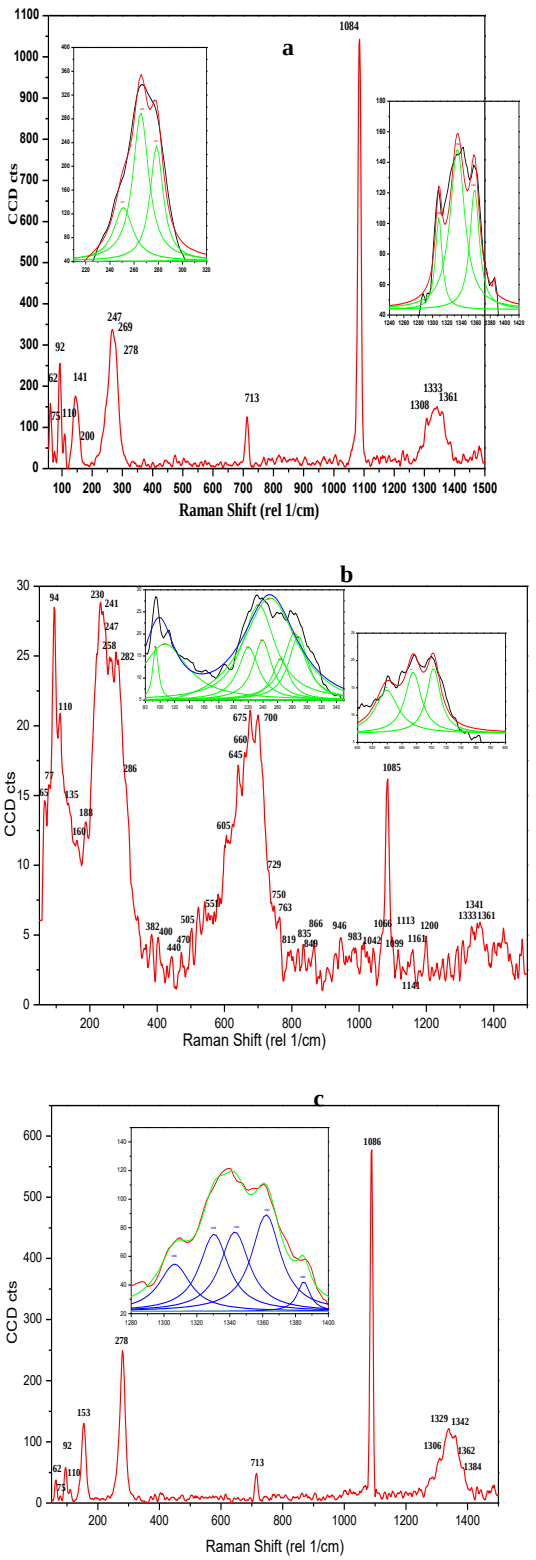

Figure 6. Raman spectra of (a) S1 the main spectra in red and de-convolution of broad bands 200 cm^{-1} to 400 cm^{-1} and 1200 cm^{-1} to 1400 cm^{-1}, (b) S2 the main spectra in red and de-convolution of broad bands 80 cm^{-1} to cm^{-1} and 600 cm^{-1} to 800 cm^{-1}, (c) S3 the main spectra in red and de-convolution of broad band 1200 cm^{-1} to 1400 cm^{-1}.

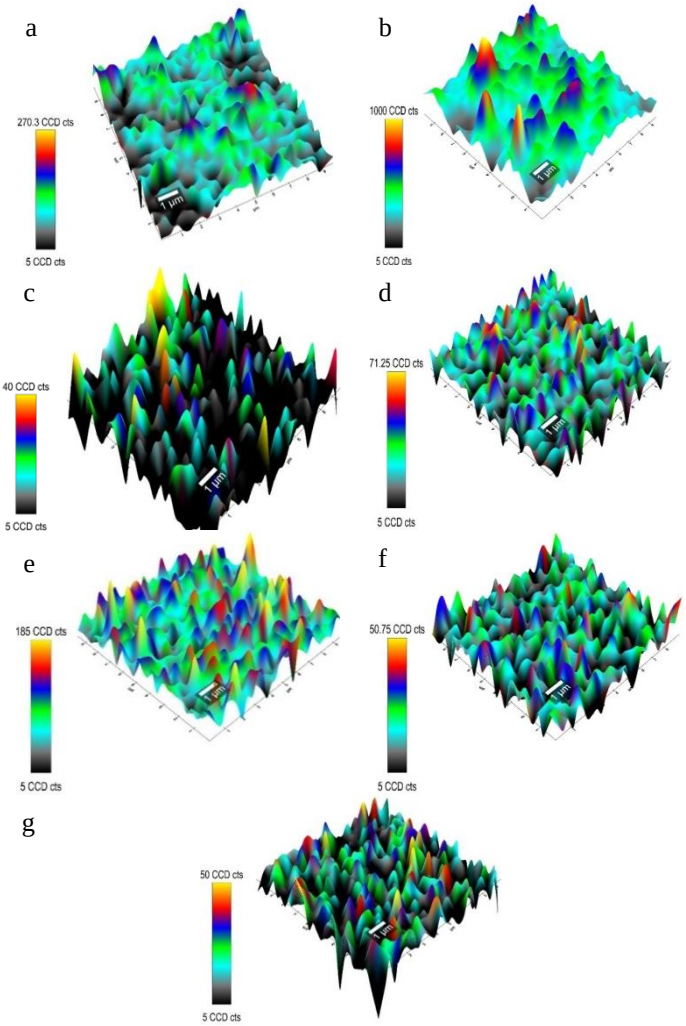

Fig. 7. The distribution of the Raman band shifted a) 278 b)1085, c) 200, d) 713, e) 62, f) 110, and g) 1333 cm-1 from the principal laser line of sample S1 which represents CaCO3, Calcite, Kaolinite, hematite, red lead, white lead, and carbon black respectively.

Table 2. Band position and assignment of the three tested samples S1, S2, and S3

Compound	Raman Bands (rel 1/cm) S1	S2	S3	ref
Calcite	1085	1085	1086	32
Calcite $CaCO_3$	278	282	278	32
SiOH		382		33
Si-O-Si		551		34
SiO_2		1066, 1099, 1200		32,35
Kaolinite ($Al_2Si_2O_5(OH)_4$)	200, 269	400, 470, 750		
Al Slilicate Si-O-Si (Al)		557,1161		36
Anhydrite ($CaSO_4$)		135, 605		(PRUFF ID: R040061)
Dolomite ($CaMg(CO_3)_2$)		174, 304, 729, 1141		
Albite Na ($AlSi_3O_8$)		330, 505, 645, 763,1113		(PRUFF ID: X050007)
Actinolite Ca–Mg–Fe^{+2}–SiO_2–OH		230,675,746,700,1029,1067		(PRUFF ID: R050025)
Hematite Fe_2O_3	247, 713, 1308	221,247,286,660,819	713,1314,1306	32,37-39
Pb_3O_4	62, 141	65	62, 153	40,41
PbO	72, 92	77, 94	75, 92	42
$2PbCO_3$•Pb $(OH)_2$	110	110	110	40
PbS		440, 835, 849, 1042		
Carbon Black	1333, 1361	1333, 1341, 1361	1329,1342,1362	33

In Figure 7(b) the distribution of Calcite is continuous with a high concentration reach to 1000 counts in a few regions coded with yellow color but the dominating color is the green and blue color representing around 500 and 650 counts respectively.

Kaolinite is present in the sample but in contradiction with both Calcite, Kaolinite is not distributed equally over the sample but it is distributed comb like or island like distribution as it is clear in Figure 7(c). In the (d) section of Figure 7 hematite distribution over the sample S1, tends to become homogeneous and cover the whole surface, the concentrations over the surface are not dominated by only one color or two like the previous compounds but we have in this spectral range (5 cm^{-1} band width centered at 713 cm^{-1}). The presence of lead compounds like Pb_3O_4, and $2PbCO_3Pb(OH)_2$ have been noticed in Figures 7(e) and (f) with homogeneous and complete coverage over the surface without any black areas could be attributed to the pollution, the same could be said about the presence of carbon black.

Sample S2 mapping is presented in Figure 8. Lead sulfide has good coverage over the sample as it is clear in Figure 8(j) the same for carbon black in section (k). The coverage of calcite is not like in sample S1 but in S2 its distribution is troughed with uncovered areas coded with black in Figures 8(a) and (b) with approximately the same concentration. But the silicate components are approximately the same concentration as Aluminum silicate, Kaolinite, Albite, and Actiniolite, in sections (c), (d), (e), and (f). The distribution of every mineral is not covering the whole area but one could easily notice that the whole area is covered with at least one silicate mineral.

The same takes place for the carbonate minerals like calcite and dolomite which being presented in Figure 8(h).

The hematite distribution that appeared in Figure 8(i) looks the same as sample S1.

Lead compounds represented in lead sulfide were presented in section (j) with good coverage but their concentration seems not high that the highest count is 20 counts. Also, the carbon black is well distributed with moderate concentrations.

Like the sample S1 the used laser is more powerful than that used in S2 this means that the counts should be higher even if the concentration is the same.

Figure 9(a) shows the calcite distribution the surface morphology is not flat but our point of research is the chemical composition in this image we could easily see a lot of areas coded with yellow color which means that the counts in these areas is around 850 counts.

The valleys' color was dominated by cyan with counts around 290 counts the less here in counts could be attributed as the valleys are out of focus not to the concentration.

The same could be noticed in Figure 9(b) for the Calcite with hills counts reach to 134 counts, and valleys around 70 counts.

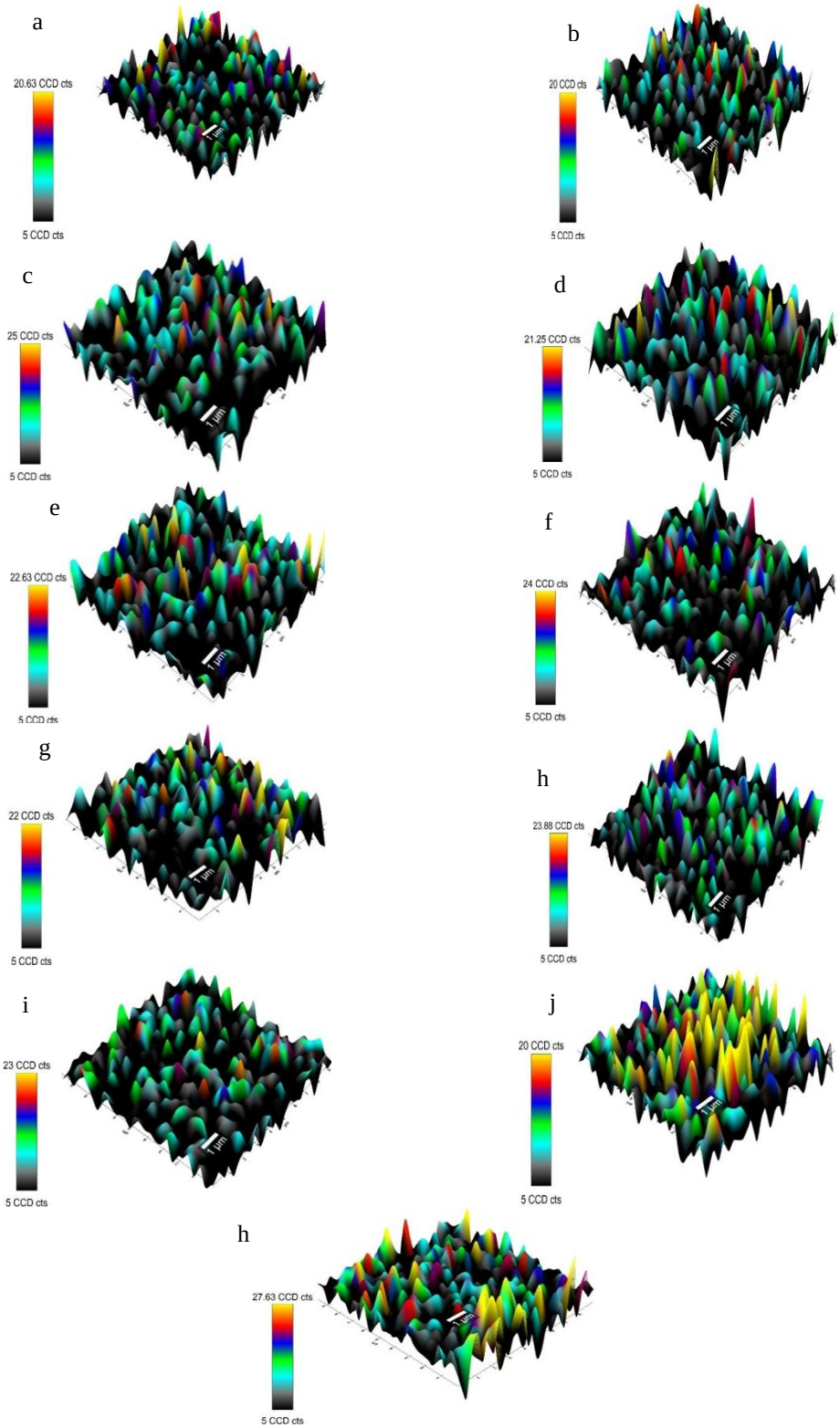

Fig. 8. The distribution of the Raman band shifted a)278, b) 1086, c) 1161, d) 470, e)1113, f)1067, g)1200, h)729, i)286, j) 1042 and k)1341 cm-1 from the principal laser line of sample S2 which represents Calcium Carbonate, Aluminum Silicate, Kaolinite, Albite, Actiniolite, Silicon Dioxide, Dolomit, Hematite, Lead Sulfide, Carbon black respectively.

Fig. 10. The distribution of the Raman band shifted a)1086, b)278, c) 713, d)153, e)92, f)110 and, g)1392 cm-1 from the principal laser line of sample S3 which represents Calcite, Dolomite, Hematite, red Lead, Lead Monoxide, white Lead, and Carbon black respectively.

3.3. Scanning electron microscope with EDX:

SEM examination was performed for both S1 and S2. Figure 10 presents the deterioration in the internal structure of each of them, especially S2, showing an irregular distribution of the sample components in addition to the large gaps and interstitial spaces as it is clear in the different magnification micro graphs in Figures 10(a), (b), and (c).

In Figures 10(d), (e), and (f) it is clear that S1 has less amount of space and random distribution of its components. The EDX analysis shows the elemental contents of the tested samples, the elements' weight according to EDX could be monitored in Table 3. It is clear from Table 2 and Figure 11 the domination of calcium as a normal result according to the origin of the pyramid rocks. Figure 11(a) shows a strong calcium signal beside signals of sodium, chlorine, and iron on the other hand Figure 11(b) presents the EDX spectrum of S2 which also shows a strong calcium signal beside signals of sodium, magnesium, sculpture, and iron.

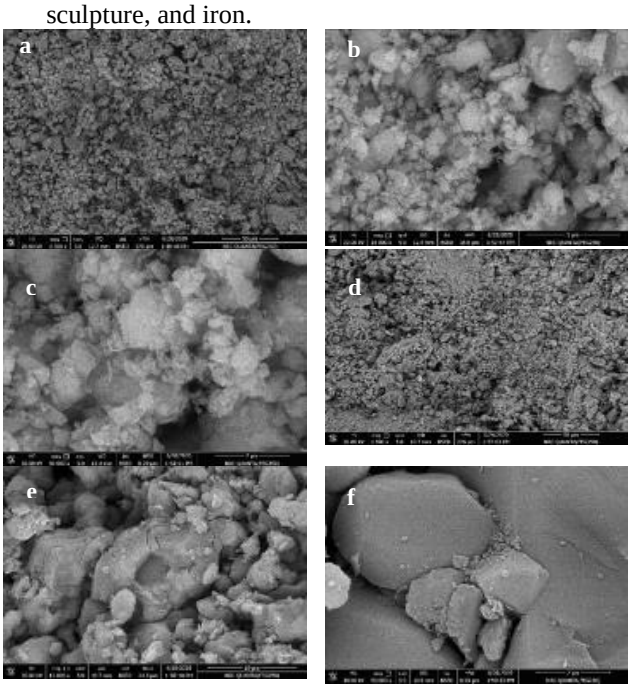

Fig. 10. SEM microscopic examination and micro structure for S1 with magnification (a) 1500X, (b) 23000X, (c) 50000X and for S2 with magnification (d) 1500X, (e) 12000X, (f) 50000X

3.4. Analysis by X-ray diffraction:

As it is clear in Figure 12 and Table 4 the XRD analysis confirms the presence of calcite, quartz, and dolomite. These results coincide with the previously introduced Raman analysis which show that calcite $CaCO_3$ and Dolomite $CaMg(CO_3)_2$ were detected in S1, S2, and S3 as a major component.

The origin of dolomite could be formed chemically from the deposition and burial of calcium limestone [13].The local and climatic environments have a clear effect on the state of preservation of the pyramid of Queen Hetep Heres, both have an ancient effect from the age of the pyramid itself, where the general weakness of the samples taken from the rock-cut part. This part bears all the characteristics of the Giza plateau that suffers from sustainable problems related to the nature of its local characteristics. In addition to the harmful effect of climatic factors, whether the effect of wind or the fluctuation between temperature and humidity, especially with the weakness of the internal structure resulting from the presence of the minerals sensitive to moisture (of different sources) and the presence of unstable dolomite and anhydrite.

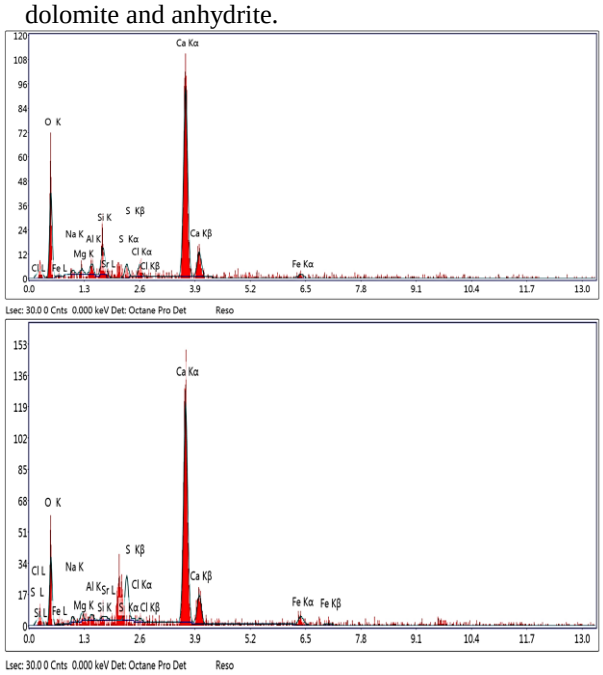

Fig. 11. EDX spectrum of (a) S1 (b) S2

Table 3.Elements weights in samples S1 and S2 as measured by EDX

Element	Weight %		Atomic %	
	S1	S2	S1	S2
O K	52.95	45.14	72.32	66.17
NaK	2.34	2.18	2.22	2.23
MgK	1	1.5	0.9	1.45
AlK	1.53	0.98	1.24	0.85
SiK	2.81	0.36	2.19	0.3
SrL	0.86	0.61	0.21	0.16
S K	0.85	4.82	0.58	3.52

ClK	1.22	0.42	0.75	0.28
CaK	34.61	39.7	18.87	23.23

FeK	1.82	4.3	0.71	1.8

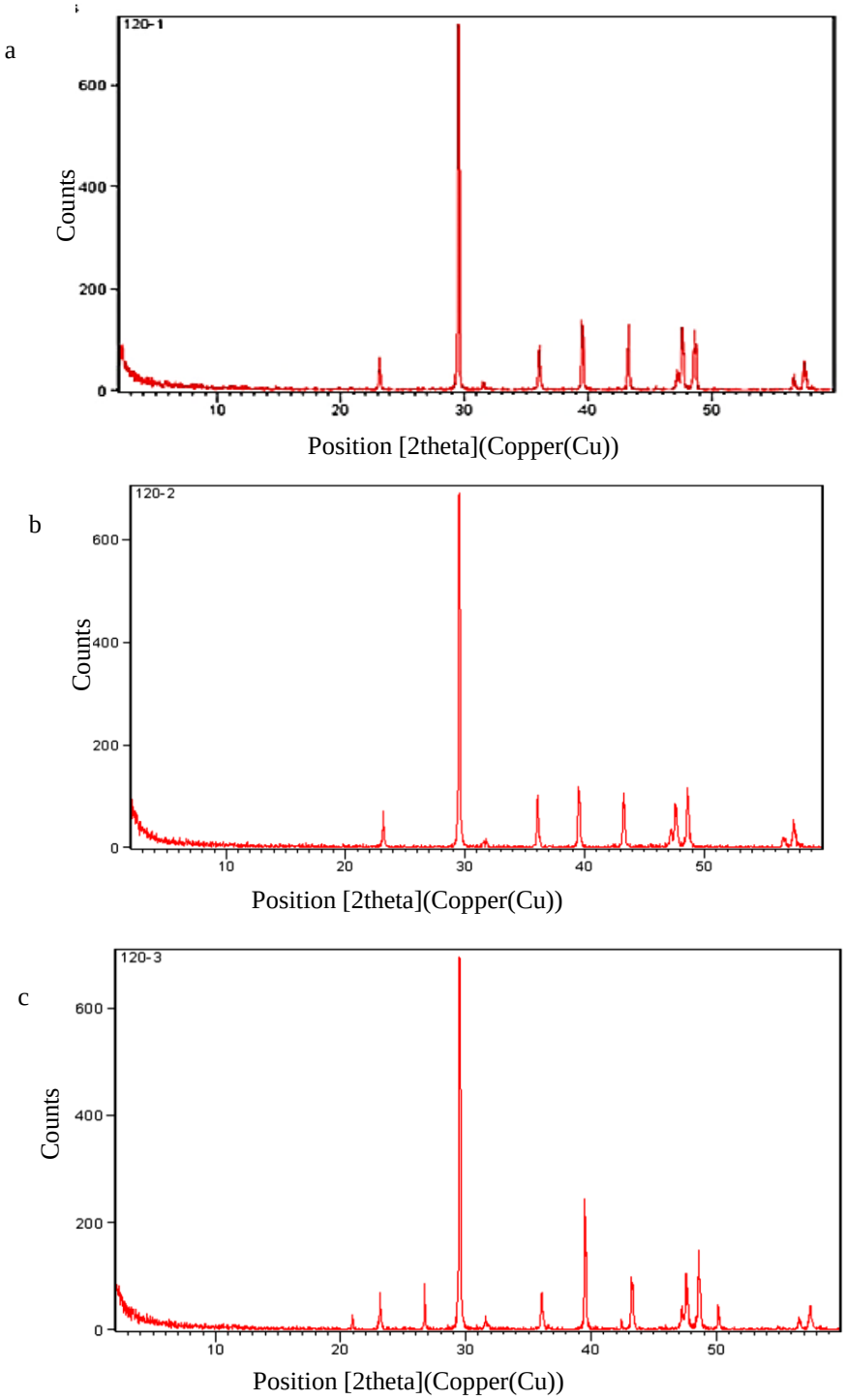

Fig. 12. The XRD patterns of samples (a) S1, (b) S2, and (c) S3

While the climatic factors explain the external appearance of the pyramid in terms of losing large parts of its structure, even if the climatic factor is not responsible for all the missing parts, it helps in the continuity of erosion and deterioration of both the constructed and carved parts of the pyramid. Besides changes in particles' size can cause deformation of the rock units. In addition to the microscopic examination and the scanning electron microscope, which showed that the samples contain proportions of organic residues and halite salts that are soluble in water, all of this negatively affects the properties of building materials and weakens their internal

structure with the passage of time and the influence of surrounding climatic factors.

Wind action facilitates the physical union between sand and limestone in the presence of humidity, especially in the winter season.. Therefore, when analysing external samples, silicon and silicon dioxide compound appear.
Looking and discussing the EDX data beside the SEM, stero microscope and even the bright field microscope will generate such question, sample S1 and S2 are compared while the silica content in S1 is more proeminent in sample, why ?
The answer of this question depends on the nature and positions of the three samples, S1was taken from the outside of the pyramid and it is normal to contain silicon and silicon dioxide as a reason of its constant exposure to sand due to the nature of the surrounding environment and wind action. While the sand is not from the contents of the rocks itself.

Table 4: Minerals Identified in S1, S2 and S3 by XRD analysis

Sample	Ref. Code	Minerals	Formula	Semi Quant [%]
S1	01-089-1304	Calcite, magnesium, syn	$CaMg(CO_3)_2$	99
	01-082-0511	Quartz, syn	SiO_2	1
S2	01-089-1304	Calcite, magnesium, syn	$CaMg(CO_3)_2$	100
S3	01-089-1304	Calcite, magnesium, syn	$CaMg(CO_3)_2$	90
	01-085-0865	Quartz, syn	SiO_2	10

4. Conclusions

Optical microscopy shows clearly the effect of environmental factors on the health state of the rocks. The study relied on using the Raman micro spectroscopy to determine the components of the main building materials in the pyramid of Hetep Heres.

This is carried out through imaging, analysis and mapping of the distribution of the components in the studied samples. This study also shows the optimum laser power that could be used during the analysis of such rocks. Raman analysis showed the presence of clay minerals like kaolinite, albite, and actinolite whose distribution increases mainly as we go deeper below the ground level (especially the burial chamber). Raman spectrum showed also the presence of anhydrite mineral that easily turns into gypsum in wet conditions or in contact with groundwater.

Therefore, the study confirms the need to provide a suitable buffer zone for the pyramid of the Queen Hetep Heres to limit the effect of direct friction by visitors to the outer part of the pyramid. An important result is to customize the visit to the burial chamber so that the high number of visitors does not cause an increase in humidity levels inside the pyramid in addition to the need for continuous monitoring of the rates of indoor temperature and humidity to provide a stable environment that limits further deterioration.

A very important result from this study is the confirmation of the urgent need for continuing the evacuation of the surrounding habitant and development plans for the Giza Plateau in general to limit the impact of its sustainable problems on its archaeological buildings.

Acknowledgments:
The authors would like to show their gratitude to the Giza Antiquities Zone and the laboratories of the Restoration Department at the Faculty of Archeology-Cairo University, the Egyptian Mineral Resources Authority (Ministry of Petroleum and Mineral Resource) and the Center for Research, for their abundant assistance, proposals and facilities.

5. Conflict of interest:

The authors announce that they have no conflict of interest.

6. References

[1] C. L. N. Ruggles, *Monuments of the Giza Plateau*, New York, Springer Science+Business Media, **2015**.
[2] M. Bárta, *Cambridge Archaeological Journal*, **2005**; 15, 177-191. doi:10.1017/S0959774305000090.
[3] G.A. Reisner, *A history of the Giza necropolis*, Massachusetts, Harvard University press, **1955**.
[4] A. Siliotti, *Guide to the pyramids of Egypt*, Barnes & Noble Books, **1997**.
[5] S. W. Morsy, A. H. Mohamed, *JECA*, **2015**, 9,1191-1201. doi: 10.17265/1934-7359/ 2015.10.007.
[6] A. Yaseen, *International Journal on: Proceedings of Science and Technology*, **2018**, 1, 97:108. https://doi.org/10.21625/resourceedings.v1i2.326.
[7] S. Hemeda, A. Sonbol, *Heritage Sci.*, **2020**, 8, 8. https://doi.org/10.1186/s40494-020-0356-9.
[8] M. E. Lehner, *Archaeology of an Image: The Great Sphinx of Giza, A Dissertation Presented to the Faculty of the Graduate School of Yale University in Candidacy for the Degree of Doctor of Philosophy Volume 1,* Ann Arbor (Mich.) : UMI, **2011.**

[9] T. Aigner, *N. Jb. Geol. Paläont. Abh.*, **1983,** 166, 347-368.
[10] https://www.weather- atlas.com/en/egypt-climate 2021
[11] S. Agrawala, M. Annett, El R. Mohamed, C. Declan, Van A. Maarten, H. Marca, S. Joel, *Development and climate change in Egypt: focus on coastal resources and the Nile*, OECD,**2004.**
[12] https://www.climatestotravel. com/climate/egypt 2021
[13] A. Ali, E. Al-Banna, *Study of the archaeological building materials on Farasan Islands, Kingdom of Saudi Arabia, and their relationship with the islands' local and climatic environment, the 3rd international Conference on Defence Sites: Heritage and Future*, WIT Transactions on The Built Environment, 158, **2016**.
[14] Atta D., Ismail M.M., Battisha I.K., Opt. Laser Technol., **2022**, 149, 107761, DOI: 10.1016/j.optlastec.2021.107761
[15] D. Atta, A. Fakhry, M. Ibrahim. *Der Pharma Chemica*, **2015,** 7, 357-361.
[16] N. M. Farrage, A. H. Oraby, E. M. M. Abdelrazek, D. Atta, *Biointerface Res. Appl. Chem.*, **2019,** 9, 3934-3941.
[17] Elbanna, A., Atta, D., Sherief, D., Dent. Res. J. **2022**, 19, 1, https://dx.doi.org/10.4103%2F1735-3327.336686.
[18] F.H. Elbatal, A.M. Abdelghany, H.A. Elbatal, Spectrochem. Acta A, **2014**, 122, 461–468, https://doi.org/10.1016/j.saa.2013.11.011
[19] D. Atta, A. Okasha, *Spectrochem. Acta A.*, **2015**, 135, 1173-1179, https://doi.org/10.1016/j.saa.2014.07. 085
[20] D. Atta, A. Okasha, M. Ibrahim, *Der Pharma Chemica*, **2016,** 8,76-82.
[21] O. Osman, A. Mahmoud, D. Atta, A. Okasha, M. Ibrahim, *Der Pharma Chemica*, **2015,** 7, 377-380.
[22] M. Ibrahim, H. Elhaes, D. Atta, *JCTN*, **2017,** 14, 4114-4117, https://doi.org/ 10.1166/jctn.2017.6794
[23] A. Okasha, D. Atta, W. M. Badawy, M. V. Frontasyeva, H. Elhaes, M. Ibrahim, *JCTN.*, **2017,**14, 1357-1361, https://doi.org/10. 1166/jctn.2017.6457.
[24] D. Atta, F. Gomaa, H. Elhaes, M. Ibrahim, *JCTN*, **2017,** 14, 2405-2408, https://doi.org/ 10.1166/jctn.2017.6840.
[25] Analytical Methods Committee. AMCTB No 67, *Analytical Methods*, 7, 4844, **2015**. https://doi.org/10.1039/c5ay90036k
[26] M. C. Caggiani, C. Philippe, *Phys. Sci. Rev.*, **2018,** 3, 20180007.
[27] P. Colomban, *JRS*, 49, 921–34, **2018**. https://doi.org/ 10.1002/jrs.4042.
[28] F. Izzo, G. Chiara, G. Celestino, L. Alessio, M. Mariano, *Infrared Physics & Technology*, 106, 103266, **2020**. https://doi.org/10.1016/j.infrared.2020.103266
[29] A. Refaat, D. Atta, O. Osman, A. A. Mahmoud, S. El-Kohadary, W. Malek , M. Ferretti, H. Elhaes, M. Ibrahim, *Biointerface Res. Appl. Chem.*,**2019** 9, 4685-4698, https://doi.org/10.33263/ BRIAC96.685698.
[30] D. Chiriu, F. A. Pisu, P. C. Ricci, C. M. Carbonaro, *Materials*, **2020**, 13, 2456, https://doi.org/10.3390/ma13112456.
[31]N. M. Farrage, A. H. Oraby, E. M. Abdelrazek, D. Atta, *Egypt. J. Chem.*, **2019** 62, 99-109, https://doi.org/ 10.21608/ejchem.2019.12746.1791
[32] P. Colomban, *JRS*,**2012**, 43, 1529–1535, https://doi.org/ 10.1002/jrs.4042.
[33] P. Vandenabeele, H.G.M. Edwards, J. Jehlička, *Chem. Soc. Rev.*,**2014**, 43, 2628–49, https://doi.org/ 10.1039/C3CS60263J
[34]G. Gouadec, L. Bellot-Gurlet, D. Baron, P. Colomban, in *Raman imaging, techniques & applications Vol. 168*, Berlin, Springer Series in Optical Sciences, **2012**.
[35] C. Miliani, F. Rosi, B. G. Brunetti, A. Sgamellotti, *Acc. Che. Res.*, **2010,** 43, 728–38, https://doi.org/10.1021/ar100010t.
[36] S. V. Stefanovsky, K. M. Fox, J. C. Marra, *Mater. Res. Soc. Symp. Proc.*,**2013**, 1518, 53–58, https://doi.org/10.1557/opl.2013.143
[37] M. Moskovits, *JRS*, **2005**, 36, 485–96, https://doi.org/10. 1002/jrs.1362
[38] P. Colomban, V. Milande, H. Lucas, *JRS*,**2004**, 35, 68–72, https://doi.org/ 10.1002/jrs.1085
[39] D. A. Long, *Raman Spectroscopy*, New York, McGraw-Hill International Book Company, **1977**.
[40] D. A. Long, *The Raman effect: a unified treatment of the theory of Raman scattering by molecules*, Chichester, John Wiley & Sons Ltd, **2002**.
[41] B. Lucia, J. H. C. Robin, F. Steven, *Analyst*,**2001**, 126, 222–227, doi: 10.1039/b008302j.